PHYSICAL REVIEW B **107**, 104415 (2023)

Editors' Suggestion

Lattice dynamics and in-plane antiferromagnetism in $Mn_xZn_{1-x}PS_3$ across the entire composition range

Robert Oliva,[1,2,*] Esther Ritov,[3] Faris Horani,[3] Iñigo Etxebarria,[4] Adam K. Budniak,[3] Yaron Amouyal,[5]
Efrat Lifshitz,[3] and Mael Guennou[1]
[1]*Department of Physics and Materials Science, University of Luxembourg, 41 rue du Brill, L-4422 Belvaux, Luxembourg*
[2]*Geosciences Barcelona (geo3bcn-CSIC), Lluis Sole I Sabaris S/N, 08028 Barcelona, Catalonia, Spain*
[3]*Schulich Faculty of Chemistry, Solid State Institute, Russell Berrie Nanotechnology Institute, Helen Diller Quantum Center, Nancy and Stephen Grand Technion Energy Program, Technion–Israel Institute of Technology, Haifa 3200003, Israel*
[4]*Fisika Saila and EHU Quantum Center, Euskal Herriko Unibertsitatea UPV/EHU,*
Sarriena Auzoa z/g, 48940 Leioa, Basque Country, Spain
[5]*Department of Materials Science and Engineering, Technion–Israel Institute of Technology, Haifa 3200003, Israel*

(Received 4 November 2022; revised 15 February 2023; accepted 21 February 2023; published 16 March 2023)

Alloyed $Mn_xZn_{1-x}PS_3$ samples have been grown covering the whole compositional range and studied by means of Raman spectroscopy at temperatures from 4 to 850 K. Our results, supported by superconducting quantum interference device magnetic measurements, allowed us, on one hand, to complete the magnetic phase diagram of $Mn_xZn_{1-x}PS_3$ and establish $x \geqslant 0.3$ as the composition at which the alloy retains antiferromagnetism and, on the other hand, to identify the Raman signatures indicative of a magnetic transition. The origin of these Raman signatures is discussed in terms of spin-phonon coupling, resulting in the appearance of low- and high-frequency phonon modes. For the alloy, an assignation of the first- and second-order modes is provided with the aid of first-principles lattice-dynamical calculations. The compositional dependence of all phonon modes is described, and the presence of zone-folded modes is shown to take place for the alloy. Finally, a comparison of the Raman spectra of $ZnPS_3$ to other compounds of the transition metal phosphorus trisulfide family allowed us to conclude that low-frequency phonon peaks exhibit an abnormally large broadening. This is consistent with previous claims on the occurrence of a second-order Jahn-Teller effect that takes place for $ZnPS_3$ and Zn-rich $Mn_xZn_{1-x}PS_3$.

DOI: 10.1103/PhysRevB.107.104415

I. INTRODUCTION

The family of layered transition metal phosphorus trichalcogenides (TMPTs) gained renewed interest due to its unique magnetic properties together with excellent chemical and structural stability [1]. While early studies were devoted to the understanding of the crystal structure, intercalation properties [2], and their applicability as cathodes for lithium batteries [3], it was later shown that TMPTs exhibit a plethora of types of two-dimensional (2D) magnetic ordering. This is interesting from both fundamental and applied perspectives due to their potential for designing multifunctional materials and flexible electronics based on heterostructures and alloys [4]. Despite the high technological interest, TMPTs are scarcely investigated compared with other 2D families such as transition metal dichalcogenides.

Transition metal phosphorus trisulfides with the chemical formula MPS_3 (M typically being Mn, Fe, Co, Ni, Zn, or Cd) crystallize into the monoclinic layered structure that corresponds to the $C2/m$ space group. Single-layer MPS_3 consists of a cation metal (M^{2+}) arranged in a honeycomb array sandwiched between the chalcogen planes, while the adjacent layers are held by weak van der Waals S-S interlayer interactions [5,6]. Aside from robust chemical stability at ambient conditions, magnetic properties can be tuned via cation exchange by using divalent magnetic metal cations such as Mn^{2+}, Fe^{2+}, or Ni^{2+}, which exhibit short-range spin ordering at temperatures higher than the critical temperature. The magnetic properties of TMPTs are determined by the number of up spins and their magnetic moment arrangement within a single layer. Spins mainly arrange antiferromagnetically (AFM) with Néel [5,7], stripy [8,9], or zigzag [10] disposition of first next-neighbor (NN) spins. Importantly, superexchange interactions with second and third NNs are not negligible and aid in controlling the magnetization stabilization resulting in Néel temperatures (T_N) in the range from 78 K for $MnPS_3$ up to 155 K for $NiPS_3$ [11].

Alloying allows covering a wide band-gap range, further increasing the range of applicability of TMPTs, spanning from 1.6 eV for magnetically active $NiPS_3$ up to 3.4 eV for diamagnetic $ZnPS_3$. The band gap in bulk compounds is either direct or quasidirect, and its nature depends on the degree of ionicity of the transition metal element. The impact of alloying magnetically ordered MPS_3 into a diamagnetic matrix has been scarcely investigated. Early studies [12] evaluated the effect of alloying and temperature on the magnetic susceptibility for $Fe_xZn_{1-x}PS_3$ ($0 < x \leqslant 1$) and reported an increase

---

[*] roliva@geo3bcn.csic.es

of the Néel temperature upon increasing iron concentration. Dilution of spin-$\frac{5}{2}$ Mn^{2+} ions on a diamagnetic host lattice of $CdPS_3$ showed that Mn(II) substitutionally replaces Cd and exhibits a high degree of covalency with NN sulfur ligands [13]. Later studies investigated the $Mn_xZn_{1-x}PS_3$ alloy throughout the whole compositional range and confirmed that Zn cations randomly substitute in the crystal lattice [14]. Additionally, the compositional effect on T_N was also evaluated for a few samples, and the spin-flip field was investigated [15,16]. These works allowed us to conclude that the first NN exchange is found to be independent of composition, while the critical concentration for long-range order was estimated to be 45% Mn. These effects were suggested to strongly impact the magnetic phase diagram, so it is highly desirable to evaluate magnetic ordering along the whole compositional range.

Raman spectroscopy is a powerful tool to investigate not only the vibrational and structural properties of 2D systems but also determine magnetic texture in 2D magnetic materials. Temperature-dependent Raman experiments on MPS_3 ($M =$ Ni or Fe) and their alloyed compounds revealed rich Raman features below T_N due to magnetic ordering. These effects were classified into three categories: (i) folding of the Brillouin zone (BZ) due to the presence of magnetic ordering, (ii) spin-spin and spin-phonon interactions, and (iii) interference of the single-phonon state with electronic transitions due to the spin splitting of the electronic band structure [17–20]. While the AFM ordering in these compounds results in a doubled magnetic cell in the in-plane directions as well as a doubling in the out-of-plane direction for $FePS_3$, for the case of $MnPS_3$, the chemical and magnetic unit cell sizes coincide, so no folded modes are expected [2,20–24].

In this paper, we provide a comprehensive study on the effect of alloying magnetically active $MnPS_3$ into a diamagnetic matrix ($ZnPS_3$) to shed light on the magnetic, vibrational, and structural properties of alloyed TMPTs. $Mn_xZn_{1-x}PS_3$ is particularly interesting from a fundamental perspective because, from one side, $MnPS_3$ is a true 2D AFM (Heisenberg type, as determined from neutron diffraction measurements [25], with a spin angle of $\approx 8^\circ$ from the out-of-plane direction [26]) that exhibits Néel-type magnetic ordering (i.e., spins are flipped between NNs, and the resulting magnetic point group is $2'/m$) [10] at least down to the bilayer limit [27], and adjacent layers are coupled ferromagnetically (FM) [26] with proven magnon-spintronics capabilities [28]. On the other hand, $ZnPS_3$ is diamagnetic and might exhibit a distorted crystal lattice while maintaining a similar band gap and lattice parameters to those of $MnPS_3$. Previous experiments showed that a similar compound $CdPS_3$, which belongs to the same group of Zn (i.e., the IIb group), exhibits a distorted crystal lattice and a structural transition at $T = 228$ K [29–31], so temperature-dependent measurements on $ZnPS_3$ are desirable. Finally, it is particularly interesting to research $Mn_xZn_{1-x}PS_3$ from a lattice-dynamical perspective because its cation average atomic number (from $Z = 25$ for Mn up to $Z = 30$ for Zn) covers those of the most relevant MPS_3's (i.e., $FePS_3$, $CoPS_3$, and $NiPS_3$), which could reveal valuable information with regard to the relative impact of (i) the reduced atomic mass and (ii) the electronic configuration on the Raman spectrum.

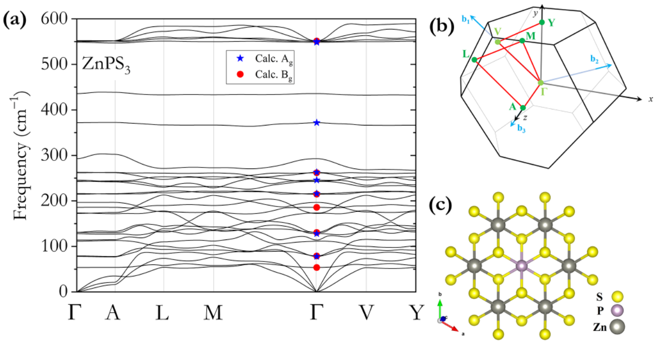

FIG. 1. (a) Calculated phonon dispersion curves of bulk $ZnPS_3$. Calculated frequencies of the A_g and B_g modes are shown as blue and red symbols, respectively. (b) First Brillouin zone (BZ) with selected high-symmetry points together with the k-path used for the phonon dispersion curves (PDCs; red lines). (c) The top view of a $ZnPS_3$ slab is represented using VESTA software [28].

II. RESULTS AND DISCUSSION

A. Lattice-dynamical calculations

Bulk $MnPS_3$ and $ZnPS_3$ are layered compounds with ABC-type stacking. The corresponding space group is monoclinic $C2/m$, and the point group is C_{2h}. This structure gives rise to 15 Raman-active modes from the irreducible representation $\Gamma = 8A_g + 6A_u + 7B_g + 9B_u$. There are eight A_g modes (here labeled from A_{g1} to A_{g8}) which can be probed under parallel scattering configuration [e.g., $z(xx)\bar{z}$ in the conventional setting] and seven B_g modes (here labeled from B_{g1} to B_{g7}) which are active in cross-scattering configuration [e.g., $z(xy)\bar{z}$].

For $ZnPS_3$, the calculated frequencies and corresponding phonon dispersion curves (PDCs) are shown in Fig. 1 (calculated phonon frequencies of A_g and B_g modes are included as star and circle symbols, respectively). From the figure, very flat dispersion curves can be observed for the optical phononic branches [the chosen k-path is shown in Fig. 1(b) with red lines and includes representative high-symmetry k-points], giving rise to a large phonon gap in the 330–540 cm^{-1} region. This is in good agreement with previous lattice-dynamical calculations based on phenomenological models and reflects the distinct nature of the high-frequency modes (i.e., >250 cm^{-1}), involving ion movements of the P_2S_6 octahedral cage, from that of the low-frequency modes (i.e., <250 cm^{-1}), involving phonons with strong contributions of the heavy metal ions and phosphorus atoms [2]. However, while those calculations predicted a flat dispersion for the high-frequency modes, our first-principles calculation methods revealed that the frequency of the mode with the highest frequency A_{g8} significantly increases (by up to ≈ 35 cm^{-1}) at the border of the BZ. For the case of monolayers, calculations based on density functional theory (DFT) predicted a similar increase in the frequency of the highest-frequency mode in the M high-symmetry point for a slab, which is equivalent to the V point in the $C2/m$ bulk structure [22].

The phonon dispersion curves of $MnPS_3$ and frequencies of the A_g and B_g modes are shown in Fig. 2 (calculated frequencies of A_g and B_g modes are included as star and circle symbols, respectively). Like $ZnPS_3$, a very flat phononic dispersion can be observed for most phononic branches, and a

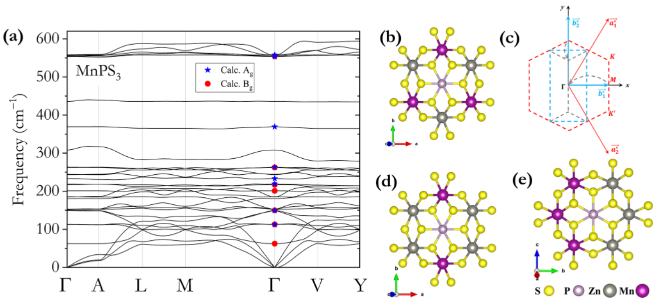

FIG. 2. (a) Calculated phonon dispersion curves of bulk $MnPS_3$. Calculated frequencies of the A_g and B_g modes are shown as blue and red symbols, respectively. (b) Top view centered around phosphorus of a $MnZnP_2S_6$ slab (note that this mixed crystal corresponds to a composition of $Mn_{0.50}Zn_{0.50}PS_3$) with an atomic arrangement corresponding to the crystallographic space group $C2$. Such an arrangement results in (c) a zone folding of the Brillouin zone (BZ) that is equivalent to antiferromagnetically ordered $MnPS_3$. Two additional configurations of $MnZnP_2S_6$ with space groups $P2/m$ and $P2/c$ have been investigated and are plotted in (d) and (e), respectively. The unit cells of the three structures are shown in Fig. SM10 in the Supplemental Material [32].

frequency increase takes place for the highest modes at the border of the BZ. This is highly relevant for magnetically active MPS_3 compounds since, below the Néel temperature, zone-folding phenomena induced by the elastic Bragg magnetic scattering from the spin superstructure are expected for phonon modes that either modulate the spin-orbit coupling or the exchange interaction [19]. While zone-folding phenomena are not expected to take place for $MnPS_3$, here, it is expected to take place for perfectly ordered and alloyed $MnZnP_2S_6$. The corresponding metal-related zone-folding phenomenon is schematically shown in Fig. 2(c) for a slab with a rectangular unit cell of the form $M_4P_4S_{12}$ (blue) from a hexagonal $M_2P_2S_6$ structure (red).

For the case of the alloy ($[x] = 50\%$), phonon frequencies at the zone center were calculated for the three structures shown in Figs. 2(b), 2(d), and 2(e). For completeness, FM and AFM arrangements for the Mn atoms were included in the calculations. Our calculations revealed that in-plane FM and AFM ordering exhibit energetic differences in the same order as different atomic arrangements (in the order of 10 meV per 20 atoms), the AFM being systematically energetically favorable as well as the $P2/c$ structure. The least favorable structure was $P2/m$ with FM spin ordering (+67 meV for 20 atoms with respect to the $P2/c$-AFM structure).

The atomic arrangements presented in Figs. 2(b), 2(d), and 2(e) result in a decrease of symmetry from the $C2/m$ structure of the compositional end members to $P2/m$, $C2$, and $P2/c$ space groups, respectively. Consequently, the number of phonon modes is increased at Γ. For the $C2$ structure, the phonon number increase from symmetry reduction results in A_g and A_u modes of $C2/m$ becoming 16 A-symmetry modes and B_{g2} and B_{u2} becoming 14 B-symmetry modes, with a total of 27 Raman-active optical modes and three acoustic modes. On the other hand, the $P2/c$ and $P2/m$ structures exhibit a total of 60 and 58 modes, respectively (three of which are acoustic) with A_g, A_u, B_g, and B_u symmetries. Most of their phonon frequencies nearly match the average between those calculated for the pure compounds at Γ and V (all zone-center phonon frequencies of the pure compounds as well as the three mixed arrangements are included in Table SM1 in the Supplemental Material [32] for A_g and A_u symmetry-equivalent modes and in Table SM2 in the Supplemental Material [32] for B_g and B_u symmetry-equivalent modes; calculated mode frequencies at V are shown in Table SM3 in the Supplemental Material [32] for the pure compounds). Remarkably, out of the 14 optical A_g and 16 B_g calculated Raman-active modes of the $P2/c$ structure, 18 modes exhibit nearly identical frequencies to those averaged for the compositional end members at Γ and V. The frequencies of some of these modes match those of modes at different in-plane high-symmetry k-points, such as new modes at ≈33 cm^{-1} higher energies than A_{g8}, which evidences that some alloy configurations activate modes away from Γ though the zone-folding mechanism.

B. Temperature-dependent Raman measurements of $MnPS_3$ and $ZnPS_3$

Bulk $MnPS_3$ and $ZnPS_3$ are expected to give rise to 8 A_g and 7 B_g Raman-active modes. Since many of their phononic frequencies are nearly degenerate, resulting in 10 Raman peaks, these are labeled from P_1 up to P_{10}. Within this notation, these are shown for $ZnPS_3$ and $MnPS_3$ in Figs. 3(a) and 4(b), respectively, at temperatures from ambient temperature down to 4 K. The intensities of the spectra have been normalized to that of the most intense peak P_8.

While the Raman spectra of $MnPS_3$ are relatively well understood both at room and low temperatures, the Raman spectra of $ZnPS_3$ have been comparatively scarcely investigated [33,34]. Strikingly, many Raman features of $ZnPS_3$ are strongly distinctive from those of MPS_3 with $M =$ Mn, Ni, Co, or Fe. The most notorious differences from MPS_3 compounds are that $ZnPS_3$ exhibits (i) a much larger broadening of the low-frequency modes (from P_1 to P_7) at ambient temperature, (ii) a decrease in frequency from 20 cm^{-1} and up to 60 cm^{-1} for the P_2 and P_3 peaks when compared with other MPS_3's, and (iii) smaller frequency difference of the modes $P_6 - P_7$ and $P_9 - P_{10}$. This can be seen by comparing both panels of Fig. 3 as well as from Fig. SM2 in the Supplemental Material [32]. Such differences cannot be merely attributed to differences in the ionic mass or size of the metal since the atomic numbers of M^ZPS_3 compounds ($Z = 25 - 28$) are very similar to that of $ZnPS_3$ ($Z = 30$).

The remarkable difference between the Raman spectra of $ZnPS_3$ and any other TMPT can be accounted for by either of the following hypotheses: (i) the crystal lattice of $ZnPS_3$ is not $C2/m$, or (ii) the crystal lattice of $ZnPS_3$ is structurally disordered. Here, we support the latter since previous x-ray diffraction (XRD) studies on nanocrystals found that $ZnPS_3$ is isomorph to compounds of the same family [35,36]. On the other hand, octahedrally coordinated d^{10} close-shell cations such as Ag^+, Cu^+, Cd^{2+}, or Zn^{2+} typically exhibit coupling between the filled d^{10} orbitals with energetically closely lying empty s orbitals which decrease the energy barrier toward lower-symmetry geometries which is experimentally measured as large thermal parameters and positional disorder

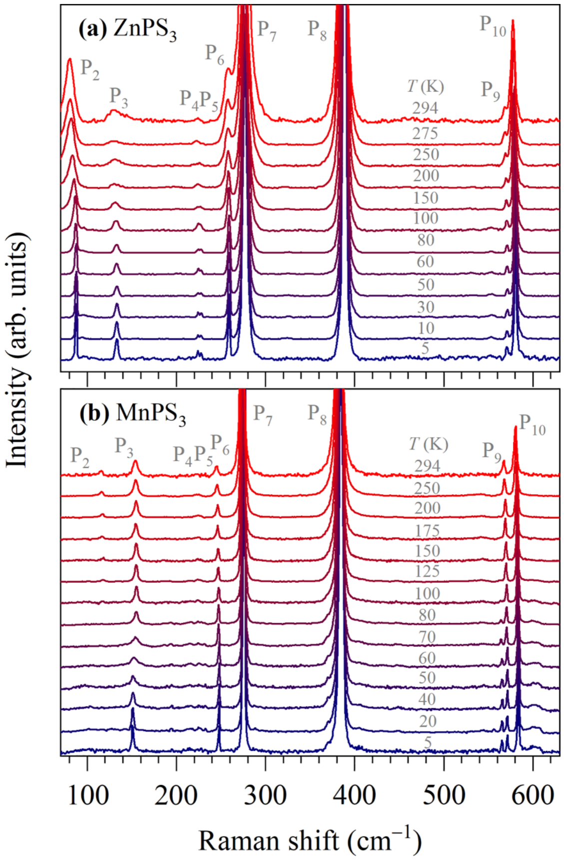

FIG. 3. Raman spectra of $ZnPS_3$ (a) and $MnPS_3$ (b) acquired at different temperatures, from ambient temperature (top spectrum) down to liquid helium temperature (bottom spectrum). First-order Raman A_g and B_g modes are labeled from P_2 up to P_{10}. A smooth background has been subtracted, and all spectra have been vertically shifted for better clarity.

(i.e., dynamic and static distortions, respectively) [37–39]. Abnormally high atomic displacement parameters (ADPs) previously measured by single-crystal x-ray measurements allowed us to confirm the presence of such a second-order Jahn-Teller effect on $CdPS_3$ and $ZnPS_3$ [36,40,41]. Moreover, a phase transition due to a rearrangement of layer stacking from the low-temperature trigonal $R3$ phase to the monoclinic $C2/m$ phase has been shown take place for $CdPS_3$ at $T = 228$ K [29–31], but no equivalent studies have been performed for $ZnPS_3$. From our Raman spectra, we conclude that the broadening of the low-frequency phonon modes, which mostly involve metallic ion displacements, is explained by the instability of Zn, in agreement with experimentally observed large ADPs [40,41]. As expected from anharmonic effects, the peak broadening increases up to 550 °C (high-temperature Raman spectra are shown in Fig. SM6 in the Supplemental Material [32]), the temperature at which the sample starts to degrade, but no abrupt changes in broadening or peak frequencies are observed, thus indicating that no structural phase transition takes place for $ZnPS_3$. On the other hand, from Fig. 3(a), the broadening of the low-frequency peaks strongly decreases at lower temperatures, and a strong increase of frequency takes place for $P2$ (i.e., $\sim$8 cm^{-1}, which is one order of magnitude higher than typical shifts for higher-frequency peaks or peaks in $MnPS_3$). This evidences that our samples are highly crystalline, no structural transition takes place, and the dynamic disorder is corrected at low temperatures. These results are in perfect agreement with our DFT calculations, which confirmed that the stable phase for $ZnPS_3$ is $C2/m$ at zero and room temperature since the potential well for Zn does not split when volumes are increased to that of $ZnPS_3$ at room temperature.

For $MnPS_3$, distinct Raman signatures abruptly show up right below the Néel temperature (as can be seen in Figs. 3(b), 4, and SM9 (top) in the Supplemental Material [32]), namely, (i) the vanishing of $P_2 \sim 117\,\text{cm}^{-1}$; (ii) four new peaks $\sim$194, 370, 565, and 605 cm^{-1}; and (iii) many very weak Raman peaks in the range 125–300. Since these peaks are not visible right above T_N, these cannot be attributed to first- or second-order Raman processes and must be inherently related to the magnetic transition, but their physical origin is unknown.

To accurately perform an assignation of all the Raman features of $MnPS_3$, a spectrum integrated with a sufficiently long time was acquired at $T = 3.4$ K, and all weak Raman features were rendered visible. This is shown in Fig. 4, together with extracted experimental peak frequencies (shown as colored ticks below the spectra) and calculated phonon frequencies (shown as colored ticks at the bottommost region of the figure). From the figure, the most prominent peaks, labeled from P_2 to P_{10}, correspond to A_g and B_g Raman-active modes (experimental frequencies are shown in Fig. 4 as red and blue ticks below the spectrum). Second-order Raman features are observed at 544 and 760 cm^{-1}, which correspond to $2A_{g5}$ (P_7) and $2A_{g6}$ (P_8) overtones, respectively, as well as 405, 430, 537, and 622 cm^{-1}, which we assign to the combination of A_g modes of $A_{g2} + A_{g4}$ ($P_3 + P_6$), $A_{g3} + A_{g5}$ ($P_3 + P_7$), $A_{g4} + A_{g5}$ ($P_6 + P_7$), and $A_{g4} + A_{g6}$ ($P_6 + P_8$), respectively (all second-order Raman peak frequencies are included as black ticks below the spectrum).

Our assignation of second-order modes is in perfect agreement with that previously reported by Peschanskii *et al.* [42], who proposed that all low-temperature weak Raman features correspond to second-order Raman processes. However, we support that the assignation of other weak features cannot be attributed to a second-order process since either those modes are not observable above T_N, or their intensity is comparable with that of second-order modes arising from the combination of the very intense P_7 and P_8 peaks. For instance, the peak at 450 cm^{-1} previously attributed to a $2A_{g3}$ overtone is observable at ambient temperature, but its intensity is in the same order of magnitude as A_{g3}, hence two orders of magnitude larger than expected for an overtone (our assigned second-order modes exhibit intensities two orders of magnitude lower than their corresponding first-order modes, as typically expected for nonresonant processes). Such a feature, visible at low temperature as well as in $ZnPS_3$ (see Fig. SM9 in the Supplemental Material [32]), is here attributed to a A_u mode either activated by disorder or by magnetic ordering (the latter effect has already been reported for $FePS_3$ [20]) since our calculations predict a very large and narrow density of states of this mode [the very flat dispersion of the corresponding phononic branch can be seen in Fig. 2(a)] at

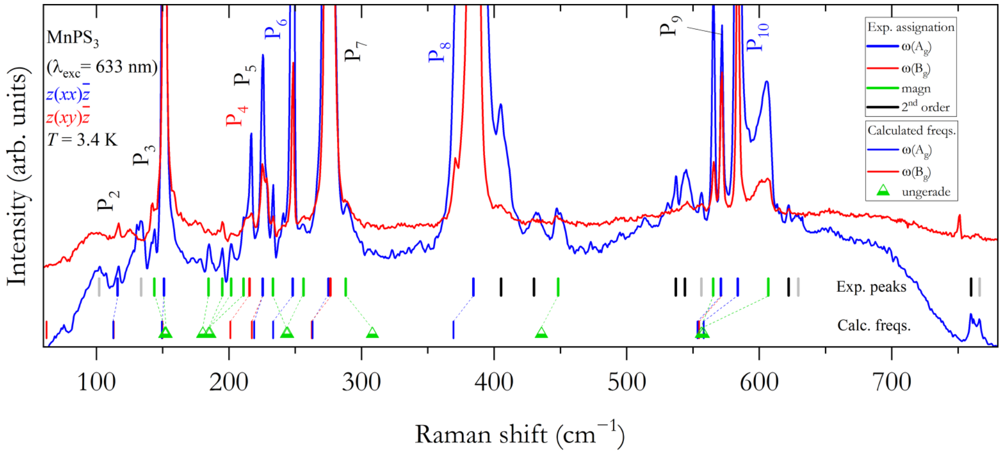

FIG. 4. Raman spectra of MnPS$_3$ acquired at a temperature of 3.4 K in parallel $z(xx)\bar{z}$ (Porto's notation) and crossed $z(xy)\bar{z}$ scattering configurations as blue and red, respectively. Characteristic peaks corresponding to A_g, B_g, and both phonon modes are labeled (P$_2$ to P$_{10}$) in blue, red, and black, respectively. The peak positions of all prominent Raman features are shown with ticks below the spectra, and their colors correspond to our assignation (dashed lines connect experimental with calculated frequencies, at the bottom-most). Most peaks been assigned to either A_g, B_g, second-order modes, or magnetically activated A_u and B_u modes in blue, red, black, and green, respectively.

a frequency of 436 cm^{-1}, which is within the −5% range of typical frequency underestimation in DFT calculations within presently used functionals.

Aside from A_g, B_g, and second-order modes, many weak Raman features show up in the 100–300 cm^{-1} region as well as ≈33 cm^{-1} above P$_{10}$ in striking resemblance with theoretically predicted frequencies at V. While zone-folding mechanisms are expected for alloyed systems, no zone-folding phenomena are expected for Néel AFM ordering in MnPS$_3$. In the AFM phase, the inversion center is lost, and the classification of the modes as gerade or ungerade is no longer valid. Phonons transform according to the magnetic correpresentations A and B of the magnetic point group $2'/m$, and the Raman tensors become like those of the nonmagnetic $C2h(m)$ point group [43]. This change of symmetry allows silent ungerade modes of the paramagnetic phase to become active, although the Raman response is likely weak for most of them.

To provide an assignation to modes activated by magnetic ordering, Fig. 4 includes calculated frequencies of ungerade modes as green triangles. While these frequencies can be assigned to the most prominent experimental peaks, unassigned peaks (marked in gray ticks in Fig. 4) correspond well to calculated zone-edge frequencies. In this regard, more theoretical and experimental work is desirable to fully understand magnetically activated Raman peaks in MnPS$_3$ and compounds of the same family. For instance, magneto-Raman measurements could reveal the presence of a magnon peak such as that found in FePS$_3$. Also, it would be desirable to experimentally probe the phononic dispersion of MnPS$_3$ by either inelastic neutron or x-ray scattering [24].

C. Temperature-dependent Raman measurements of Mn$_x$Zn$_{1-x}$PS$_3$

The Raman spectra of Mn$_x$Zn$_{1-x}$PS$_3$ are shown in Fig. 5 for the whole compositional range at ambient temperature (top panel) and liquid helium temperature (bottom panel).

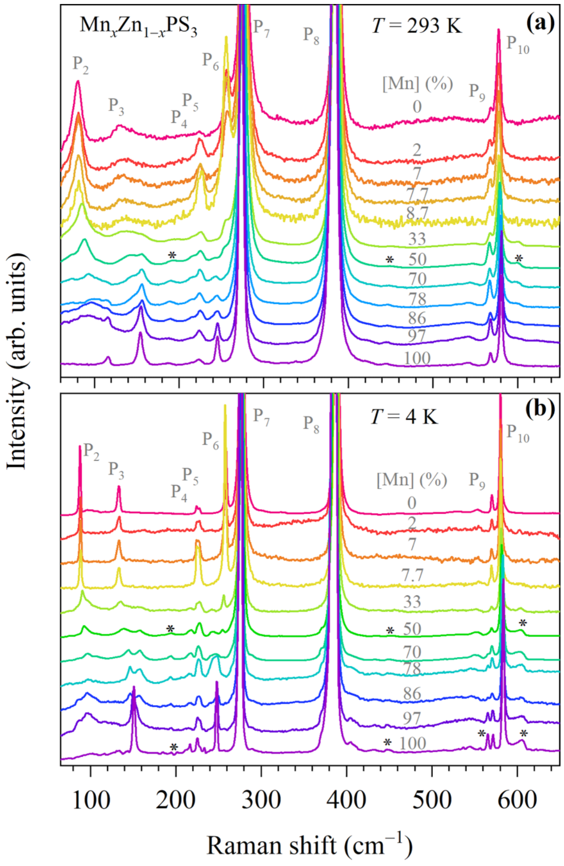

FIG. 5. Raman spectra of different samples of Mn$_x$Zn$_{1-x}$PS$_3$ covering the whole compositional range acquired at (a) ambient temperature and (b) liquid helium temperature. All first-order Raman peaks have been labeled from P$_2$ up to P$_{10}$; these correspond to A_g and/or B_g Raman modes since all spectra have been acquired under unpolarized conditions. Weak Raman features showing up at intermediate composition and below T_N for Mn-rich Mn$_x$Zn$_{1-x}$PS$_3$ have been marked with asterisks and attributed to zone-folded phonon modes arising from different mechanisms.

From the figure, the number, frequency, and intensity of the peaks depend on the particular compositional content. The splitting of peaks P_2, P_3, and P_6 can be easily observed at both ambient and low temperatures, especially for compositions ∼50%. This corresponds to an expected two-mode behavior consequence of a flat dispersion of the phononic branches and a somewhat large frequency difference of the modes between the compositional end members (phonon dispersion curves of $ZnPS_3$ and $MnPS_3$ are shown in Figs. 1 and 2, respectively). More interesting is the fact that very weak Raman features show up at ambient temperature for intermediate compositions (maximum signal is found at $x = 50\%$), which are very similar to those of $MnPS_3$ at low temperatures (marked with asterisks in Fig. 5). These features cannot be assigned to second-order processes owing to their particular frequencies and intensities not matching any two-mode combination or overtone. In this paper, we propose that these features are alloy-activated zone-folded modes in the in-plane direction. Indeed, the alloyed sample $Mn_{0.50}Zn_{0.50}PS_3$ can be regarded as a first approximation to the perfectly ordered mixed crystal (i.e., $MnZnP_2S_6$) since, at low temperatures, mean free paths of coherent phonons are typically a few orders of magnitude larger than the lattice unit cell. This hypothesis is supported by the fact that the weak Raman features of the alloy exhibit almost identical frequencies and intensities to those of the low-temperature AFM-ordered $MnPS_3$. Taking, for instance, $Mn_{0.50}Zn_{0.50}PS_3$, the zone-folded features are (i) a strong reduction of the P_2 peak, (ii) a peak at 195 cm^{-1}, (iii) a low-frequency tail of P_8, and (iv) a band ∼600 cm^{-1}, as can be seen in Fig. 5 at either ambient or low temperatures (see Fig. SM5 in the Supplemental Material [32] for an enlarged view). The only substantial difference arises from the fact that a peak 6 cm^{-1} below P_9 visible for $MnPS_3$ at low temperature is not visible for $Mn_{0.50}Zn_{0.50}PS_3$ at either ambient or low temperature.

For the particular case of compositions around $[x] = 50\%$, the broadening of the Raman peaks is strikingly similar to that of the pure compositional end members, as can be seen in Fig. 5 [for the most intense peak P_8, the full width at half maximum (FWHM) is 5 cm^{-1} for all compositions at ambient temperature]. This is because, unlike conventional bulk crystals where alloying typically increases the peak broadening by around one order of magnitude [44,45], in alloyed layered compounds, structural defects are comparatively lower, resulting in a typical peak broadening of a factor of 2 for intermediate compositions [46]. For the particular case of our $Mn_xZn_{1-x}PS_3$ samples, a small broadening factor of 1.05 at 4 K and 1.07 at ambient temperature suggests that the crystallinity is exceptionally good due to the similar size of the Mn and Zn ions, which results in each metal ion being properly contained within the octahedral S_6 cage.

To shed light on the origin of the structural anomalies of $ZnPS_3$ as well as their impact on the alloy, systematic measurements have been performed on all alloyed samples for temperatures ranging from 4 K up to ambient temperature. From Fig. 5(a), Zn-rich samples exhibit broad low-frequency peaks (from P_2 to P_7), which correspond to vibrations involving mostly the metal cations (for P_7, FWHM = 5 cm^{-1} of samples with $[Zn] > 65\%$, while FWHM = 2.6 cm^{-1} for pure $MnPS_3$ at low temperature). On the other hand, the FWHM of the high-frequency peaks, corresponding to vibrations of the P_2S_6 units, remains similar at ambient temperature to that of $MnPS_3$. The temperature and compositional dependence of the broadening of the low-frequency P_7 and high-frequency peak P_8 are shown in Figs. SM7 and SM8 in the Supplemental Material [32]. From these figures, it can be concluded that the structural distortion in $ZnPS_3$ becomes strong at temperatures >100 K and linearly decreases for samples with $[Mn] > 35\%$. Similar nonlinear structural effects have been previously reported for perovskite alloys [47,48].

For the case of Mn-rich samples, magnetic ordering plays a major role in the lattice dynamics at low temperatures. For instance, the FWHM of the high-frequency P_8 peak of $MnPS_3$ remains broad and constant ∼4 cm^{-1} below ≈120 K (see Fig. SM7(b) in the Supplemental Material [32]). We tentatively attribute such a feature to the entrance of a frustrated spin-glass phase above the Néel temperature characterized by a short-range spin-spin correlation <120 K that coincides with a maximum in the susceptibility [as discussed below, on Fig. 8(a)] [7,49], in agreement with neutron scattering measurements which revealed scattering from correlations shorter than the scale of the Bragg peaks at 100 K which were attributed to 2D critical fluctuations [50]. Previous works have shown that magnetic ordering strongly affects the frequency and intensity of peak P_3 around T_N [42,51]. Hence, P_3 can be used as a signature to estimate the Néel temperature from Raman measurements alone.

The peak frequencies of spectra in Fig. 5 have been extracted at room and liquid helium temperatures by fitting Lorentzian peaks and are plotted as a function of composition in Fig. 6. In the figure, alloy peaks P_5 and $P_7 - P_{10}$ exhibit a linear dependency between the compositional end members, while peaks P_2, P_3, and P_6 exhibit two-phonon mode behavior. For the latter case, their frequencies interpolate from the frequency of a compositional end member to the corresponding local vibrational mode (LVM). In some compositional ranges (mostly for $[Mn] > 30\%$), these peaks coexist and can be observed in the Raman spectra as doublets. From the figure, the frequencies of the peaks at low temperatures (marked as black crosses) are like those obtained at ambient temperature (marked as colored symbols), and their frequencies are slightly increased, as expected from the intrinsic thermal expansion. However, the frequency P_3 of $MnPS_3$ appears to strongly decrease at low temperatures, from an ambient frequency of 156.0 down to 151.2 cm^{-1}, which is a very similar frequency to that corresponding to the extrapolated P_3-Zn to $[Mn] = 100\%$ (i.e., the frequency of the P_3 Zn LVM is 150.2 cm^{-1}). Here, we sustain that the apparent peak shift is mostly due to a vanishing of a P_3-Mn peak, which is not allowed in the AFM ordering, simultaneously accompanied by the re-entrance of a closely lying P_3-Zn peak which is an alloylike mode. This is clearer for P_2 due to the larger separation between the frequency of the LVM (100.2 cm^{-1} at ambient temperature, $[x] = 1$) and Mn-P_2 (116.0 cm^{-1} at ambient temperature, $[x] = 1$). The Mn-P_2 peak is only active in the paramagnetic $C2/m$ structure and vanishes at both (i) low temperatures due to AFM ordering and (ii) ambient temperature with significant alloying (i.e., it vanishes for alloy concentrations $[x] < 0.75$).

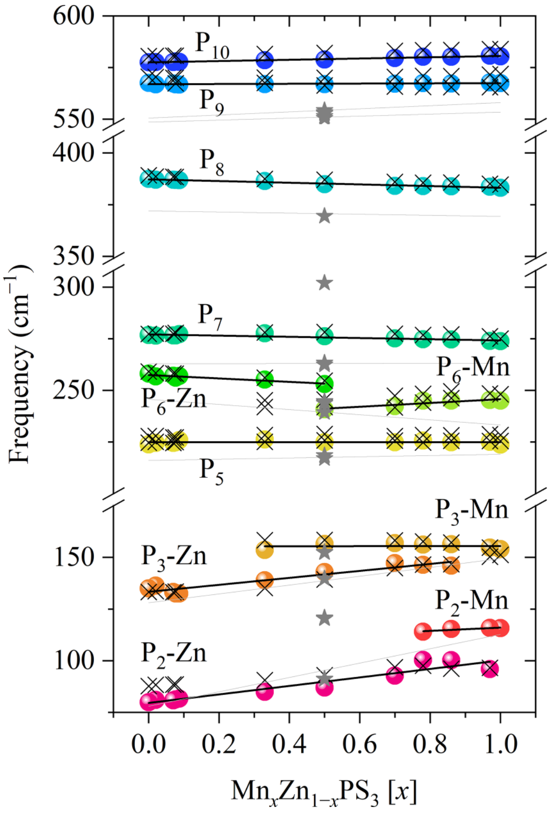

FIG. 6. Compositional dependence of the fitted frequencies of the Raman peaks as measured at ambient temperature (colored symbols) and 4 K (crosses). Linear fits are included for the data acquired at room temperature, and peak labels are included accordingly. Calculated frequencies for the compositional end members are shown with thin gray lines. Calculated frequencies for the exact composition of 0.5 are shown as gray stars. Extracted frequencies for the compositional end members are shown in Table I.

The peak frequencies shown in Fig. 6 have been linearly fitted for measurements performed at ambient and low temperatures (i.e., 4 K). Extracted experimental frequencies are provided in Table I together with the calculated figures. For comparison purposes, calculated frequencies of the A_g modes of $MnPS_3$ and $ZnPS_3$ have been linearly interpolated and plotted in Fig. 6 as thin gray lines. From the figure, our calculations underestimate the frequency values by up to −5%, especially those of modes involving the movement of light ions. A ∼5% underestimation of the optical phonon frequencies is well documented for the PBEsol functional applied to 2D compounds [52]. Figure 6 includes the calculated frequencies of the modes of perfectly mixed crystal $MnZnP_2S_6$ (a total of 15 + 14 = 29 optical modes with A and B symmetries, respectively, are shown as gray star symbols in the figure), where each metal is exchanged to first neighbors in-plane (the corresponding space group is $C2$). Calculations predict that P_5 and $P_7 - P_9$ exhibit one-mode behavior with a frequency that almost linearly interpolates between the compositional end members, while P_2, P_3, and P_6 exhibit two-mode behavior (the one- and two-mode behavior can be seen from the calculated frequencies for $[x] = 0.5$, shown as gray stars in Fig. 6), in excellent agreement with experiments.

D. Determination of the Néel temperature from Raman spectroscopy

For the Néel temperature determination in the alloy, several Raman features can be used, such as the broadening of low-frequency peaks, peak positions, the appearance and disappearance of new phonon modes due to the change of crystal symmetry from magnetic ordering, or variations in relative intensities. However, we found, in agreement with previous works [27,42,51], that the most temperature-sensitive signature arises from the frequency of the P_3-Mn

TABLE I. Experimental and calculated phonon frequencies (in units of cm^{-1}) of $MnPS_3$ (left) and $ZnPS_3$ (right). Experimental values are obtained from a linear fit of the compositional dependence of the Raman features for alloyed samples of all compositions. Experimental figures in bold correspond to peaks measured for the compositional end members.

		$MnPS_3$			$ZnPS_3$		
		Experiment			Experiment		
Peak label	Phonon mode	$T = 293$ K	$T = 10$ K	Calculations	$T = 293$ K	$T = 10$ K	Calculations
P_1	B_{g1}			62.3			53.7
P_2-Zn	A_{g1} B_{g2}				**79.6**	**87.9**	78.0 79.0
P_2-Mn	A_{g1} B_{g2}	**116.0**	—	112.9 112.9		—	—
P_3-Zn	A_{g2} B_{g3}	—	—	—	**133.4**	**132.0**	128.0 130.6
P_3-Mn	A_{g2} B_{g3}	**155.5**	**156.0**	149.5 150.1	—	—	—
P_4	B_{g4}	—	—	201.3	—	—	185.8
P_5	A_{g3} B_{g5}	**224.9**	**225.5**	219.3 217.2	**224.9**	**224.8**	216.1 214.8
P_6-Mn	A_{g4}	**245.7**	**249.0**	233.0	—	—	—
P_6-Zn	A_{g4}	—	—	—	**257.4**	**258.8**	245.7
P_7	A_{g5} B_{g6}	**274.2**	**276.4**	263.1 262.4	**277.1**	**277.8**	262.8 261.8
P_8	A_{g6}	**383.2**	**384.9**	369.3	**387.2**	**388.8**	372.0
P_9-Mn	A_{g7} B_{g7}	**567.4**	**571.2**	553.4 554.6	—	—	—
P_9-Zn	A_{g7} B_{g7}	—	—	—	566.9	570.0	548.6 551.3
P_{10}	A_{g8}	**580.6**	**584.0**	558.0	**577.5**	**580.4**	550.5

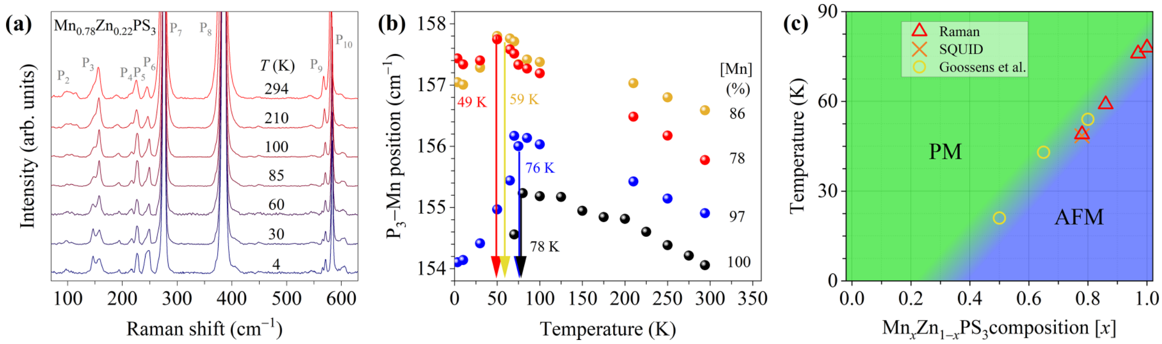

FIG. 7. (a) Raman spectra of a $Mn_{0.78}Zn_{0.22}PS_3$ sample acquired at different temperatures, from 4 K (bottom) up to ambient temperature (top). (b) Dependence on temperature of the fitted frequency of the mode P_3-Mn. (c) Magnetic phase diagram including experimental data obtained in this paper by means of Raman spectroscopy (triangles), superconducting quantum interference device (SQUID) measurements (cross), and *magnetic measurements performed by Goossens *et al.* [15] and Chandrasekharan *et al.* [14] (circles).

mode (a detailed illustration of the evolution of P_3 with temperature for $MnPS_3$ is shown in Fig. SM3 in the Supplemental Material [32]). The physical origin of the P_3 mode remains a matter of debate despite that the two-magnon hypothesis (Raman-active magnons have been observed in similar compounds such as $FePS_3$ [24]) has been ruled out due to its discrepancy in energy (i.e., 177 cm^{-1} for a two-magnon as measured by neutron diffraction studies [53], far from the experimental 154 cm^{-1} value of P_3). In this regard, a few alternative interpretations have been presented including (i) the presence of a more complex magnetic sublattice lacking magnetism for some magnetic ions [42]; (ii) a two-particle phonon-magnon excitation [42]; (iii) a spin-related magnetic-AFM phase transition resulting in the disappearance of the P_3 mode and a re-entrance of a second mode located 4 cm^{-1} below P_3 that shows up below a temperature of 50 K, close to the critical temperature of 55 K where $MnPS_3$ might exhibit Heisenberg XY-like ordering [51]; (iv) a single mode that broadens and redshifts as a consequence of spin-phonon coupling where fluctuations are responsible for disrupting the coherence of the lattice vibrational modes and shortening the lifetimes, resulting in a sharp increase of the linewidth [27]; and (v) a Fano resonance between a phonon peak and a two-magnon continuum [54]. Since Mn-rich samples exhibit a P_3 doublet [see Fig. 5(b)] with relative intensities strongly dependent on the temperature, it is clear to us that P_3 is indeed two closely lying modes with different physical origins. Hence, the apparent broadening and shift toward lower frequencies of the P_3 mode in pure $MnPS_3$ are mostly explained by the increase in the intensity of the low-frequency peak. Since the energy separation between both peaks is ∼3 cm^{-1} and their broadening is ∼4 cm^{-1} for pure $MnPS_3$ and as large as 10 cm^{-1} for a sample with [Mn] = 78%, the P_3 doublet in $MnPS_3$ is not possible to be experimentally resolved. However, while the low-frequency peak corresponds to a folded mode [with increasing intensity with reduction of temperature, as also observed for the alloy in Fig. 7(a)], the high-frequency P_3 peak is still susceptible to hybridize with the two-magnon continuum.

Following the previous argumentation, it is possible to determine T_N from variations in relative intensities between the P_3 doublet or small variations of peak frequency. The temperature-dependency of the frequency of the Mn-like P_3 peak is plotted in Fig. 7(b) for samples with [Mn] content >78%. In the figure, the frequencies increase with decreasing temperature, as expected as a consequence of thermal lattice contraction, but at a certain temperature, an abrupt decrease in frequency (and intensity) takes place, especially for the pure $MnPS_3$ compound. From this analysis, the Néel temperature decreases with lowering [Mn] content. This is expected since short-range magnetic interaction is quenched in the diamagnetic lattice. From these results, it seems clear that the Néel temperature of [Mn] > 97% is ∼78 K, and for 78% < [Mn] < 86%, T_N is 49 K. These results are in excellent agreement with our superconducting quantum interference device (SQUID) measurements: $T_N = 48.5$ K for a sample with 78% Mn content. The compositional dependence of T_N is plotted in Fig. 7(c). From this figure, excellent agreement is reached between previously [15] and presently reported SQUID measurements, measurements using a Faraday balance [14] and our Raman measurements. By linearly interpolating the phase diagram, it seems that no long-range magnetic ordering would take place for samples with [Mn] < 30%.

E. SQUID magnetic-field measurements

Magnetic susceptibilities of $MnPS_3$ and high alloying ratios of $Mn_xZn_{1-x}PS_3$ ($0 < x \leqslant 1$) were measured over a wide temperature range by a SQUID magnetometer. Figure 8(a) reveals the temperature dependences of mass magnetic susceptibilities χ of $MnPS_3$ bulk single crystal in two directions: in-plane ($\chi_{//ab}$) and out-plane ($\chi_{\perp ab}$) at a constant magnetic field (100 Oe). For bulk $MnPS_3$, each Mn^{2+} ion is coupled AFM with its nearest neighbor in the 2D plane (in-plane). The coupling between adjacent planes is FM (out-of-plane). The $MnPS_3$ AFM system exhibits a characteristic temperature, termed Néel temperature (T_N), at which the long-range magnetic order is finally lifted. Here, $T_N \sim 78$ K is determined from the discontinuity in the first derivative $(\partial\chi/\partial T)_H$ shown in Fig. 8(b). The AFM arrangement below T_N is illustrated in the inset. For $MnPS_3$, the susceptibility dependence on strength of the magnetic field can be divided into three different regions: (i) below $T_N \sim 78$ K, $\chi_{//}$ tends to zero with decreasing temperature, while $\chi_\perp$ increases gradually. The

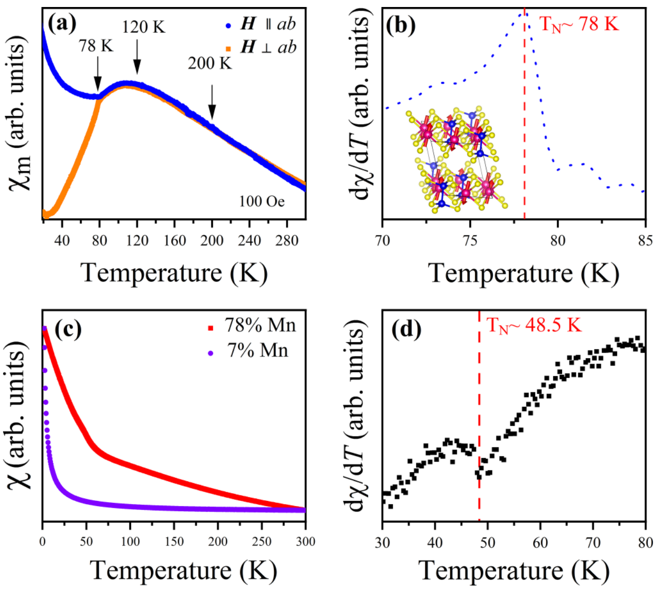

FIG. 8. Identification of the Néel transition temperature in bulk $Mn_xZn_{1-x}PS_3$ crystals. (a) Temperature dependence of the magnetic susceptibility (χ) of bulk $MnPS_3$ crystals with the magnetic field applied in-plane (blue curve) and perpendicular to the plane (orange curve). The black arrow points to the temperature below which the two curves start to deviate, which allows the Néel temperature (T_N) identification. (b) $d\chi/dT$ of the in-plane measurement in (a) with an inflection point at $T_N \approx 78$ K. The inset illustrates the antiferromagnetic spin arrangement below T_N. (c) Temperature dependence of the magnetic susceptibility of $Mn_{0.78}P_{0.22}S_3$ (red) and $Mn_{0.07}Zn_{0.93}PS_3$ (purple). The zoom area is focused on the inflection point at low temperatures. (d) $d\chi/dT$ of the in-plane measurement of $Mn_{0.78}Zn_{0.22}PS_3$ in (c) with an inflection point at $T_N \approx 48.5$ K.

anisotropic AFM order below T_N can be originated from the following: First, the range of exchange interactions is beyond the nearest neighbor, arising from a nonnegligible spin-orbit coupling. Second, the dipolar anisotropy dictates the magnetization axis and provides the system with a weak Ising character [55]. (ii) Above T_N, from 78 to 120 K, the susceptibilities behave equally, where an isotropic and broad hump is observed at 120 K ($T \sim 3/2T_N$). The broad maximum at 120 K can be explained by the change in magnetic structure, reflecting a small single-ion anisotropy order due to short-range spin-spin correlation in the *ab* plane [7,49,50], which is typical for low-dimensional or 2D magnetic systems. (iii) From 120 to 200 K and ambient temperature, a linear behavior is noted, demonstrating a paramagnetic phase order in $MnPS_3$.

Figure 8(c) displays the temperature dependence of the magnetic susceptibility of highly Mn-alloyed $Mn_{0.78}Zn_{0.22}PS_3$ ($x = 0.78$) and Mn-diluted $Mn_{0.07}P_{0.93}S_3$ ($x = 0.07$) crystals with the magnetic field applied in-plane at constant magnetic fields of 1000 and 100 Oe, respectively. For $Mn_{0.78}P_{0.22}S_3$ (red curve), the paramagnetic region is extended toward a lower temperature than $MnPS_3$, and T_N is shifted. Here, $T_N = 48.5$ K was estimated from the discontinuity in the first derivative ($\partial\chi/\partial T$) shown in Fig. 8(d). It is worth noticing that the hump in the susceptibility at $T > T_N$ vanishes, which could be explained by lowering the Mn nearest-neighbor interactions in the $Mn_{0.78}Zn_{0.22}PS_3$ system, leading to the breakdown of the short-range spin-spin correlation [15]. Below T_N, the susceptibility increases due to long-range exchange interaction. For Mn-diluted $Mn_{0.07}Zn_{0.93}PS_3$ crystal, no long-range AFM transition was observed (purple curve), as in this case a significant number of the spins no longer belong to the infinite cluster, so the magnetic susceptibility matches the behavior of a weak paramagnetic system.

III. CONCLUSIONS

We provided an assignation of the Raman-active phonon modes of $Mn_xZn_{1-x}PS_3$ and accurately described its compositional dependence in terms of one- and two-mode phonon behavior. With the aid of first-principles calculations, all Raman features have been assigned either to first-order, second-order, ungerade, or zone-folded modes. Low-temperature Raman and magnetic measurements allowed us to determine the Néel temperatures of Mn-rich $Mn_xZn_{1-x}PS_3$ samples and complete the corresponding phase diagram. Hence, we confirm that Raman spectroscopy is a valid tool to identify magnetic transitions in 2D alloyed systems, and relevant Raman signatures have been identified for $Mn_xZn_{1-x}PS_3$. Finally, we report abnormally broad low-frequency Raman peaks for $ZnPS_3$ at ambient temperature, which is consistent with previous claims on the presence of a second-order Jahn-Teller structural distortion.

IV. METHODS

A. Preparation and structural characterization

Single-crystalline $Mn_xZn_{1-x}PS_3$ ($0 \leqslant x \leqslant 1$) samples were grown via vapor transport synthesis without any transporting agent [15,56]. Selected amounts of powder elements (Zn, Mn, P, and S) were calculated to obtain ~1 g of substrate mixture. The mixture was grounded in an agate mortar and sealed in an evacuated quartz ampoule at a pressure $<3.5 \times 10^{-5}$ Torr. The reaction duration was set for 1 week and took place in a two-zone furnace with a gradient of temperature where the substrate zone was kept at 650 °C, and the cold deposition zone was at 600 °C. For pure $ZnPS_3$ crystals, lower temperatures were used, which are 600 °C for the substrate zone and 550 °C for the deposition zone. Crystals from the deposition zone were collected for further characterization. The composition of every crystal used in this paper was investigated by energy-dispersive x-ray spectroscopy (EDX) as the material from the deposition zone (i.e., recrystallized $Mn_xZn_{1-x}PS_3$) may have a different [Mn]/[Zn] ratio than the initially used substrate zone mixture. The $Mn_xZn_{1-x}PS_3$ compounds crystallized into a bulk monoclinic layered structure with a space group of *C*2/*m*. Figure 9(c) shows a side view (top panel) and top view (bottom panel) of the monoclinic crystal system. Single-crystal XRD measurements allowed us to extract the lattice parameters: $a = 6.0780$ Å, $b = 10.5332$ Å, $c = 6.7887$ Å, and $\beta = 107.122\,^\circ$ for $MnPS_3$ and $a = 5.9576$ Å, $b = 10.3252$ Å, $c = 6.7648$ Å, and $\beta = 107.182\,^\circ$ for $ZnPS_3$, in agreement with previous reports [35,36]. Abnormally high ADPs were found for the Zn atoms in $ZnPS_3$ [$U_{eq} = 0.030(1)$ Å] compared with the Mn

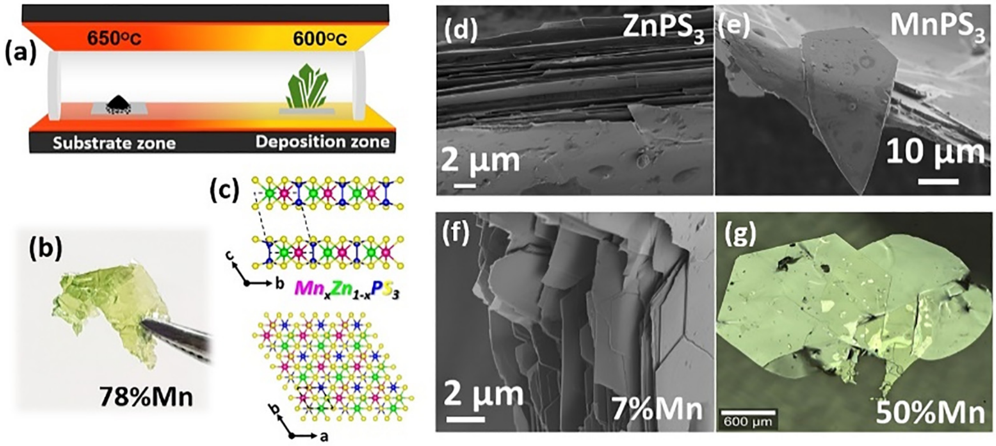

FIG. 9. Preparation and characterization of $Mn_xZn_{1-x}PS_3$ crystals. (a) Preparation method of $Mn_xZn_{1-x}PS_3$ crystals via vapor transport synthesis using a two-zone furnace. (b) A photograph $Mn_{0.78}Zn_{0.22}PS_3$ crystal seized from the deposition zone. (c) Side view and (top panel) top view (bottom panel) of the monoclinic crystal system which belongs to the $Mn_xZn_{1-x}PS_3$. (d)–(f) High-resolution scanning electron microscope (HR-SEM) images of $ZnPS_3$, $MnPS_3$, and $Mn_{0.07}Zn_{0.93}PS_3$ bulk crystals. (g) Magnified optical microscope image of $Mn_{0.5}Zn_{0.5}PS_3$ flakes.

atoms in $ZnPS_3$ [$U_{eq} = 0.01359(8)$ Å]. These values are in good agreement with those previously reported by XRD measurements [40].

B. Composition determination by EDX and scanning electron microscope morphology characterization

High-resolution scanning electron microscope (HR-SEM) images were registered with Zeiss Ultra-Plus FEG-SEM. EDX spectra were acquired with FEI E-SEM Quanta 200. Both measurements were obtained at accelerating voltage of 20 kV. EDX spectra were collected to quantitatively analyze the composition and to estimate the [Mn]/[Zn] atomic ratios of the metal in alloyed $Mn_xZn_{1-x}PS_3$ samples.

The morphology of bulk $Mn_xZn_{1-x}PS_3$ was examined using HR-SEM and an optical microscope. A selected photograph of a sample with $[x] = 78\%$ is shown in Fig. 9(b) and represents a greenish-colored crystal. Figures 9(d)–9(f) show HR-SEM micrographs of the $ZnPS_3$, $MnPS_3$, and $Mn_{0.78}Zn_{0.22}PS_3$ crystals, respectively, highlighting the layered nature of the pure and alloyed compounds. Cleavage angles of 30 ° and 60 ° can be observed, with the longest sides typically corresponding to the *b* axis. Figure 9(g) shows an optical microscope photograph of $Mn_{0.50}Zn_{0.50}PS_3$ flakes, presenting their semihexagonal shape and large surface area.

C. SQUID

SQUID measurements were performed in the Quantum Matter Research (QMR) center in the Technion using the SQUID magnetometer Quantum Design MPMS3 which provides a sensitivity of $< 5 \times 10^{-8}$ emu. Here, dc magnetic susceptibilities were measured under an externally applied field of 100 or 1000 Oe from 1.8 to 380 K.

D. Raman measurements

Raman measurements have been performed using a micro-Raman spectrometer coupled to the inVia^{TM} Reflex Raman Microscope system from Renishaw. All Raman measurements shown in this paper have been acquired in the backscattering configuration. Polarized Raman measurements have been performed under the parallel and crossed backscattering configurations as well as using different excitation energies. The 632.8-nm excitation line of a He-Ne laser was selected for all reported experiments in this paper due to its enhanced Raman signal and improved spectral resolution. Since selection rules in TMPTs are not strictly respected (see Fig. SM4 in the Supplemental Material [32]), all measurements presented in this paper were acquired in unpolarized configuration (except otherwise indicated in the figure). Low-temperature measurements have been performed using an Oxford Microstat-Hire open-cycle He cryostat together with an Oxford Mercury ITC controller. A THMS600 Linkam stage was used for the high-temperature measurements.

E. Lattice-dynamical calculations

Unit cell optimization and relaxation of atomic positions were performed by calculations based on DFT using the Vienna *Ab initio* Simulation Package, which employs a projector augmented-wave basis set [57,58]. The exchange-correlation functional revised for solids PBEsol [59] was used with the energy cutoff for plane-wave expansion set to 500 eV. Following previous DFT calculations on these compounds [10,60,61], for all the calculations, except those relative to $ZnPS_3$, the DFT + U_{eff} rotational invariant approach of Dudarev [62] was used to characterize the on-site Coulomb repulsion between the 3*d* electrons of the Mn atoms ($U_{eff} = 5$ eV). For $MnPS_3$, a Néel-type AFM order was assumed, and a convergence criterion of 5.0×10^{-4} eV/Å for the forces was used in all the relaxations. Calculations of the $ZnPS_3$ and $MnPS_3$ pure compounds were performed using the primitive cell defined as $\mathbf{a_p} = (\mathbf{a} - \mathbf{b})/2$, $\mathbf{b_p} = (\mathbf{a} + \mathbf{b})/2$, and $\mathbf{c_p} = \mathbf{c}$, where **a**, **b**, and **c** are the lattice vectors of the conventional *C*2/*m* cell as provided elsewhere [30], with a BZ integration scheme of 12 × 12 × 10. For the mixed $Mn_{0.50}Zn_{0.50}PS_3$ alloys, the conventional cell was used with a *k*-mesh of

$10 \times 7 \times 10$. For the alloys, FM and AFM orderings have been considered. In the AFM $P2/m$ and $P2/c$ structures, the two Mn atoms of the primitive unit cell are assumed to have opposite spins, and for the $C2$ structure, the spins of the two Mn atoms related by the centering are opposite. Phonon dispersion branches were calculated using the PHONOPY package [63], applying finite displacements in a supercell of $4 \times 4 \times 4$ times the primitive cell and sampling the BZ only in the Γ point.

All data derived from the experiments and calculations of this paper are available from the corresponding author upon reasonable request.

ACKNOWLEDGMENTS

F.H., E.R., and E.L. acknowledge the contribution of the QMR center and Dr. Anna Eyal for performing the SQUID measurements. The authors would like to thank Prof. Francisco Javier Zúñiga Lagares for his contribution to XRD measurements on the samples studied here. I.E. acknowledges the financial support of the "Ministerio de Ciencia e Innovación" (No. PID2019-106644GB-I00) and the Basque Country Government (No. IT1458-22). A.K.B. and E.L. were supported by the European Commission via the Marie Skłodowska-Curie action Phonsi (No. H2020-MSCA-ITN-642656).

R.O. wrote the paper and performed the low-temperature Raman experiments and data analysis. I.E. carried out first-principles calculations and contributed to the theoretical part. E.R. and A.K.B synthesized compounds under the supervision of Y.A. The SQUID magnetic measurements were performed by E.R. and F.H. and contributed to the methods section. M.G. and E.L. planned and coordinated the research. All authors discussed the results and commented on the paper.

The authors declare no competing financial or nonfinancial interests.

---

[1] V. P. Ningrum, B. Liu, W. Wang, Y. Yin, Y. Cao, C. Zha, H. Xie, X. Jiang, Y. Sun, S. Qin *et al.*, Recent advances in two-dimensional magnets: Physics and devices towards spintronic applications, Research **2020**, 1768918 (2020).

[2] M. Bernasconi, G. L. Marra, G. Benedek, L. Miglio, M. Jouanne, C. Julien, M. Scagliotti, and M. Balkanski, Lattice dynamics of layered MPX_3 (M = Mn, Fe, Ni, Zn; X = S, Se) compounds, Phys. Rev. B **38**, 12089 (1988).

[3] R. Brec, D. M. Schleich, G. Ouvrard, A. Louisy, and J. Rouxel, Physical properties of lithium intercalation compounds of the layered transition-metal chalcogenophosphites, Inorg. Chem. **18**, 1814 (1979).

[4] B. L. Chittari, Y. Park, D. Lee, M. Han, A. H. MacDonald, E. Hwang, and J. Jung, Electronic and magnetic properties of single-layer MPX_3 metal phosphorous trichalcogenides, Phys. Rev. B **94**, 184428 (2016).

[5] F. Wang, T. A. Shifa, P. Yu, P. He, Y. Liu, F. Wang, Z. Wang, X. Zhan, X. Lou, F. Xia *et al.*, New frontiers on van der Waals layered metal phosphorous trichalcogenides, Adv. Funct. Mater. **28**, 1802151 (2018).

[6] T. Song, Z. Fei, M. Yankowitz, Z. Lin, Q. Jiang, K. Hwangbo, Q. Zhang, B. Sun, T. Taniguchi, K. Watanabe *et al.*, Switching 2D magnetic states via pressure tuning of layer stacking, Nat. Mater. **18**, 1298 (2019).

[7] P. A. Joy and S. Vasudevan, Magnetism in the layered transition-metal thiophosphates MPS_3 (M = Mn, Fe, and Ni), Phys. Rev. B **46**, 5425 (1992).

[8] J. R. Morey, A. Scheie, J. P. Sheckelton, C. M. Brown, and T. M. McQueen, $Ni_2M_3O_8$: Complex antiferromagnetic order on a honeycomb lattice, Phys. Rev. Mater. **3**, 014410 (2019).

[9] E. K.-H. Lee, R. Schaffer, S. Bhattacharjee, and Y. B. Kim, Heisenberg-Kitaev model on the hyperhoneycomb lattice, Phys. Rev. B **89**, 045117 (2014).

[10] N. Sivadas, M. W. Daniels, R. H. Swendsen, S. Okamoto, and D. Xiao, Magnetic ground state of semiconducting transition-metal trichalcogenide monolayers, Phys. Rev. B **91**, 235425 (2015).

[11] Y. Yacoby, H. Zhou, R. Pindak, and I. Božović, Atomic-layer synthesis and imaging uncover broken inversion symmetry in $La_{2-x}Sr_xCuO_2$ films, Phys. Rev. B **87**, 014108 (2013).

[12] J. P. Odile, J. J. Steger, and Aaron. Wold, Preparation and properties of the solid solution series zinc iron phosphorus trisulfide ($Zn_{1-x}Fe_xPS_3$) ($0 < x < 1$), Inorg. Chem. **14**, 2400 (1975).

[13] E. Lifshitz and A. H. Francis, Analysis of the ESR spectrum of manganese(II) impurity centers in the layered compound cadmium phosphide sulfide ($CdPS_3$), J. Phys. Chem. **86**, 4714 (1982).

[14] N. Chandrasekharan and S. Vasudevan, Dilution of a layered antiferromagnet: Magnetism in $Mn_xZn_{1-x}PS_3$, Phys. Rev. B **54**, 14903 (1996).

[15] D. J. Goossens and T. J. Hicks, The magnetic phase diagram of $Mn_xZn_{1-x}PS_3$, J. Phys. Condens. Matter **10**, 7643 (1998).

[16] D. J. Goossens, A. J. Studer, S. J. Kennedy, and T. J. Hicks, The impact of magnetic dilution on magnetic order in $MnPS_3$, J. Phys. Condens. Matter **12**, 4233 (2000).

[17] M. Balkanski, K. P. Jain, R. Beserman, and M. Jouanne, Theory of interference distortion of Raman scattering line shapes in semiconductors, Phys. Rev. B **12**, 4328 (1975).

[18] G. Güntherodt, Light scattering in magnetic semiconductors, J. Magn. Magn. Mater. **11**, 394 (1979).

[19] G. Güntherodt, W. Bauhofer, and G. Benedek, Zone-Boundary-Phonon Raman Scattering in VI_2 due to Modulation of Exchange Interaction, Phys. Rev. Lett. **43**, 1427 (1979).

[20] M. Balkanski, M. Jouanne, G. Ouvrard, and M. Scagliotti, Effects due to spin ordering in layered MPX_3 compounds revealed by inelastic light scattering, J. Phys. C Solid State Phys. **20**, 4397 (1987).

[21] M. Balkanski, M. Jouanne, and M. Scagliotti, Magnetic ordering induced raman scattering in $FePS_3$ and $NiPS_3$ layered compounds, Pure Appl. Chem. **59**, 1247 (1987).

[22] A. Hashemi, H.-P. Komsa, M. Puska, and A. V. Krasheninnikov, Vibrational properties of metal phosphorus trichalcogenides from first-principles calculations, J. Phys. Chem. C **121**, 27207 (2017).

[23] J.-U. Lee, S. Lee, J. H. Ryoo, S. Kang, T. Y. Kim, P. Kim, C.-H. Park, J.-G. Park, and H. Cheong, Ising-type magnetic ordering in atomically thin $FePS_3$, Nano Lett. **16**, 7433 (2016).

[24] A. McCreary, J. R. Simpson, T. T. Mai, R. D. McMichael, J. E. Douglas, N. Butch, C. Dennis, R. Valdés Aguilar, and A. R. Hight Walker, Quasi-two-dimensional magnon identification in antiferromagnetic $FePS_3$ via magneto-raman spectroscopy, Phys. Rev. B **101**, 064416 (2020).

[25] K. Kurosawa, S. Saito, and Y. Yamaguchi, Neutron diffraction study on $MnPS_3$ and $FePS_3$, J. Phys. Soc. Jpn. **52**, 3919 (1983).

[26] E. Ressouche, M. Loire, V. Simonet, R. Ballou, A. Stunault, and A. Wildes, Magnetoelectric $MnPS_3$ as a candidate for ferrotoroidicity, Phys. Rev. B **82**, 100408(R) (2010).

[27] K. Kim, S. Y. Lim, J. Kim, J.-U. Lee, S. Lee, P. Kim, K. Park, S. Son, C.-H. Park, J.-G. Park *et al.*, Antiferromagnetic ordering in van der Waals 2D magnetic material $MnPS_3$ probed by raman spectroscopy, 2D Mater. **6**, 041001 (2019).

[28] W. Xing, L. Qiu, X. Wang, Y. Yao, Y. Ma, R. Cai, S. Jia, X. C. Xie, and W. Han, Magnon Transport in Quasi-Two-Dimensional van der Waals Antiferromagnets, Phys. Rev. X **9**, 011026 (2019).

[29] E. Lifshitz, A. H. Francis, and R. Clarke, An ESR and x-ray diffraction study of a first-order phase transition in $CdPS_3$, Solid State Commun. **45**, 273 (1983).

[30] F. Boucher, M. Evain, and R. Brec, Phase transition upon d^{10} Cd^{2+} ordering in $CdPS_3$, Acta Crystallogr. B **51**, 952 (1995).

[31] C. Sourisseau, R. Cavagnat, M. Evain, and R. Brec, Raman evidence for a phase transition in $CdPS_3$, J. Raman Spectrosc. **27**, 185 (1996).

[32] See Supplemental Material at http://link.aps.org/supplemental/10.1103/PhysRevB.107.104415 for additional Raman spectra and tables of calculated phonon frequencies.

[33] A. J. Martinolich, C.-W. Lee, I.-T. Lu, S. C. Bevilacqua, M. B. Preefer, M. Bernardi, A. Schleife, and K. A. See, Solid-state divalent ion conduction in $ZnPS_3$, Chem. Mater. **31**, 3652 (2019).

[34] C. Sourisseau, J. P. Forgerit, and Y. Mathey, Vibrational study of layered $ZnPS_3$ compounds intercalated with $[Co(\eta^5 - C_5H_5)_2^+]$ and $[Cr(\eta^6 - C_6H_6)_2^+]$ cations, J. Phys. Chem. Solids **44**, 119 (1983).

[35] G. Ouvrard, R. Brec, and J. Rouxel, Structural determination of some MPS_3 layered phases ($M =$ Mn, Fe, Co, Ni and Cd), Mater. Res. Bull. **20**, 1181 (1985).

[36] E. Prouzet, G. Ouvrard, and R. Brec, Structure determination of $ZnPS_3$, Mater. Res. Bull. **21**, 195 (1986).

[37] L. Kang, M. Zhou, J. Yao, Z. Lin, Y. Wu, and C. Chen, Metal thiophosphates with good mid-infrared nonlinear optical performances: A first-principles prediction and analysis, J. Am. Chem. Soc. **137**, 13049 (2015).

[38] R. Brec, G. Ouvrard, and J. Rouxel, Relationship between structure parameters and chemical properties in some MPS_3 layered phases, Mater. Res. Bull. **20**, 1257 (1985).

[39] R. Brec, Review on structural and chemical properties of transition metal phosphorous trisulfides MPS_3, Solid State Ion. **22**, 3 (1986).

[40] F. Boucher, M. Evain, and R. Brec, Second-order Jahn-Teller effect in $CdPS_3$ and $ZnPS_3$ demonstrated by a non-harmonic behaviour of Cd^{2+} and $Zn^{2+}d^{10}$ ions, J. Alloys Compd. **215**, 63 (1994).

[41] V. Zhukov, F. Boucher, P. Alemany, M. Evain, and S. Alvarez, Electronic structure, chemical bonding, and Jahn-Teller distortions in $CdPS_3$, Inorg. Chem. **34**, 1159 (1995).

[42] A. V. Peschanskii, T. Ya. Babuka, K. E. Glukhov, M. Makowska-Janusik, S. L. Gnatchenko, and Yu. M. Vysochanskii, Raman study of a magnetic phase transition in the $MnPS_3$ single crystal, Low Temp. Phys. **45**, 1082 (2019).

[43] A. P. Cracknell, Scattering matrices for the raman effect in magnetic crystals, J. Phys. C Solid State Phys. **2**, 500 (1969).

[44] V. Yu. Davydov, I. N. Goncharuk, A. N. Smirnov, A. E. Nikolaev, W. V. Lundin, A. S. Usikov, A. A. Klochikhin, J. Aderhold, J. Graul, O. Semchinova *et al.*, Composition dependence of optical phonon energies and raman line broadening in hexagonal $Al_xGa_{1-x}N$ alloys, Phys. Rev. B **65**, 125203 (2002).

[45] R. Oliva, J. Ibáñez, R. Cuscó, R. Kudrawiec, J. Serafinczuk, O. Martínez, J. Jiménez, M. Henini, C. Boney, A. Bensaoula *et al.*, Raman scattering by the E_{2h} and A_1(LO) phonons of $In_xGa_{1-x}N$ epilayers ($0.25 < x < 0.75$) grown by molecular beam epitaxy, J. Appl. Phys. **111**, 063502 (2012).

[46] Y. Chen, D. O. Dumcenco, Y. Zhu, X. Zhang, N. Mao, Q. Feng, M. Zhang, J. Zhang, P.-H. Tan, Y.-S. Huang *et al.*, Composition-dependent raman modes of $Mo_{1-x}W_xS_2$ monolayer alloys, Nanoscale **6**, 2833 (2014).

[47] R. Vilarinho, D. J. Passos, E. C. Queirós, P. B. Tavares, A. Almeida, M. C. Weber, M. Guennou, J. Kreisel, and J. A. Moreira, Suppression of the cooperative Jahn-Teller distortion and its effect on the raman octahedra-rotation modes of $TbMn_{1-x}Fe_xO_3$, Phys. Rev. B **97**, 144110 (2018).

[48] J. Blasco, J. García, J. Campo, M. C. Sánchez, and G. Subías, Neutron diffraction study and magnetic properties of $LaMn_{1-x}Ga_xO_3$, Phys. Rev. B **66**, 174431 (2002).

[49] A. R. Wildes, S. J. Kennedy, and T. J. Hicks, True two-dimensional magnetic ordering in $MnPS_3$, J. Phys. Condens. Matter **6**, L335 (1994).

[50] A. R. Wildes, M. J. Harris, and K. W. Godfrey, Two-dimensional critical fluctuations in $MnPS_3$, J. Magn. Magn. Mater. **177–181** 143 (1998).

[51] Y.-J. Sun, Q.-H. Tan, X.-L. Liu, Y.-F. Gao, and J. Zhang, Probing the magnetic ordering of antiferromagnetic $MnPS_3$ by Raman spectroscopy, J. Phys. Chem. Lett. **10**, 3087 (2019).

[52] J. Ibáñez, T. Woźniak, F. Dybala, R. Oliva, S. Hernández, and R. Kudrawiec, High-pressure raman scattering in bulk HfS_2: Comparison of density functional theory methods in layered MS_2 compounds ($M =$ Hf, Mo) under compression, Sci. Rep. **8**, 12757 (2018).

[53] A. R. Wildes, B. Roessli, B. Lebech, and K. W. Godfrey, Spin waves and the critical behaviour of the magnetization in $MnPS_3$, J. Phys. Condens. Matter **10**, 6417 (1998).

[54] T. T. Mai, K. F. Garrity, A. McCreary, J. Argo, J. R. Simpson, V. Doan-Nguyen, R. V. Aguilar, and A. R. H. Walker, Magnon-phonon hybridization in 2D antiferromagnet $MnPSe_3$, Sci. Adv. **7**, eabj3106 (2021).

[55] A. R. Wildes, H. M. Rønnow, B. Roessli, M. J. Harris, and K. W. Godfrey, Static and dynamic critical properties of the quasi-two-dimensional antiferromagnet $MnPS_3$, Phys. Rev. B **74**, 094422 (2006).

[56] A. K. Budniak, N. A. Killilea, S. J. Zelewski, M. Sytnyk, Y. Kauffmann, Y. Amouyal, R. Kudrawiec, W. Heiss, and E.

Lifshitz, Exfoliated $CrPS_4$ with promising photoconductivity, Small **16**, 1905924 (2020).

[57] G. Kresse and J. Hafner, *Ab initio* molecular dynamics for liquid metals, Phys. Rev. B **47**, 558 (1993).

[58] G. Kresse and J. Furthmüller, Efficient iterative schemes for *ab initio* total-energy calculations using a plane-wave basis set, Phys. Rev. B **54**, 11169 (1996).

[59] J. P. Perdew, A. Ruzsinszky, G. I. Csonka, O. A. Vydrov, G. E. Scuseria, L. A. Constantin, X. Zhou, and K. Burke, Restoring the Density-Gradient Expansion for Exchange in Solids and Surfaces, Phys. Rev. Lett. **100**, 136406 (2008).

[60] J. Yang, Y. Zhou, Q. Guo, Y. Dedkov, and E. Voloshina, Electronic, magnetic and optical properties of $MnPX_3$ (X = S, Se) monolayers with and without chalcogen defects: A first-principles study, RSC Adv. **10**, 851 (2020).

[61] M. Birowska, P. E. Faria Junior, J. Fabian, and J. Kunstmann, Large exciton binding energies in $MnPS_3$ as a case study of a van der Waals layered magnet, Phys. Rev. B **103**, L121108 (2021).

[62] S. L. Dudarev, G. A. Botton, S. Y. Savrasov, C. J. Humphreys, and A. P. Sutton, Electron-energy-loss spectra and the structural stability of nickel oxide: An LSDA + U study, Phys. Rev. B **57**, 1505 (1998).

[63] A. Togo and I. Tanaka, First principles phonon calculations in materials science, Scr. Mater. **108**, 1 (2015).